ROYAL SOCIETY OF CHEMISTRY

PAPER

Check for updates

Tailoring a multilayer fine-grained solid electrolyte interphase by pulse electrochemical activation maneuver for stable Si/C anodes†

Changhaoyue Xu,[a] Peng Jing,[a] Pengfei Xia,[a] Ye Jia,[a] Jianan Peng,[a] Qiujie He,[a] Qingqing Liu,[b] Zimo Song,[a] Xuemei Zhang,[c] Fanglin Wu,[d] Xianyu Liu, [ID][e] Kaipeng Wu,[af] Yun Zhang [ID] *[af] and Wenlong Cai [ID] *[af]

Silicon (Si) is widely regarded as one of the most promising anode materials for lithium-ion batteries due to its exceptionally high specific capacity. However, the significant volumetric change (up to 400%) of the Si anode degrades the solid–electrolyte interphase (SEI) and significantly hinders its practical application. Herein, we modulate the formation of fine-grained SEI composed of multiple layers by using a pulse electrochemical activation mode, where each layer is uniformly distributed with fine inorganic particles and interspersed with buffer organics. This tailored multilayer fine-grained SEI effectively promotes the lithium-ion diffusion kinetics through the SEI featuring a small Gibbs free energy (0.235 eV), which is only 1/5 of the typical double-layer SEI, as well as smaller charge transfer resistances during the whole electrochemical processes. Moreover, it exhibits a high Young's modulus of 12.5 GPa in comparison to that of the typical double-layer SEI (5.1 GPa) and much-inhibited stress and strain, so as to generate lower thickness expansion/shrinkage ratios. Consequently, the assembled Si/C‖LiFePO$_4$ full cell, operating at a current density of 1 A g^{-1}, demonstrates a remarkable capacity retention of 93.6% after 583 cycles, which also shows a practical application by powering an unmanned aircraft. This interfacial engineering maneuver sheds light on enhancing the electrochemical performance of other high-capacity electrode materials with substantial volume changes.

Broader context

Despite the great achievements that have been made by designing the bilayer solid electrolyte interphase (SEI), it still remains a tremendous challenge to further improve the mechanical properties and ion diffusion kinetics of the SEI layer on Si-based materials. In this work, we innovatively designed a fine-grained SEI layer through a meticulously controlled pulsed electrochemical activation strategy, marking the first application of this approach to optimize the electrochemical kinetics and long-term stability of Si/C anodes. By precisely modulating the pulse parameters, the multiple-layer fine-grained SEI is well constructed and consists of uniform fine inorganic particles (such as LiF and Li$_3$N) in each layer and interspersed with buffer oligomer organics. Benefiting from the fine-grain strengthening effect, the constructed SEI not only features enhanced rigidity and flexibility characteristics to accommodate the volume changes, but also achieves a much smaller Gibbs free energy to promote Li$^+$ diffusion kinetics. Notably, this pulsed electrochemical activation maneuver bridging the gap between fundamental interfacial science and practical battery applications not only offers a novel and scalable pathway for interface engineering, but also presents a promising and industrially viable strategy for improving cycle stability in commercial lithium-ion batteries.

[a] *Department of Advanced Energy Materials, College of Materials Science and Engineering, Sichuan University, Chengdu, 610064, China. E-mail: y_zhang@scu.edu.cn, caiwl@scu.edu.cn*

[b] *College of Polymer Science & Engineering, State Key Laboratory of Polymer Materials Engineering, Sichuan University, Chengdu, 610064, China*

[c] *Institute of Smart City and Intelligent Transportation, Southwest Jiaotong University, Chengdu, 610032, China*

[d] *State Key Laboratory of Advanced Technology for Materials Synthesis and Processing, Wuhan University of Technology, Wuhan 430070, China*

[e] *Bailie School of Petroleum Engineering, Lanzhou City University, Lanzhou 730070, China*

[f] *Engineering Research Center of Alternative Energy Materials and Devices, Sichuan University, Chengdu 610064, China*

† Electronic supplementary information (ESI) available. See DOI: https://doi.org/10.1039/d5ee02060c

Introduction

Driven by social progress, the demand for environmentally friendly, high-capacity batteries is growing, and silicon (Si) stands out among the anode materials due to its high theoretical specific capacity (4200 mA h g^{-1}).[1,2] However, the substantial volumetric expansion (approximately 400%) leads to continuous reshaping of the vital solid–electrolyte interphase (SEI), resulting in electrolyte depletion and loss of active materials.[3,4] Constructing stable SEI layers to maintain the Si particle integrity has been demonstrated as an efficient method, which has made great strides.

Research in this area has primarily focused on two key strategies: first, pre-constructing an artificial coating layer on the surface of Si-based materials to serve as the SEI film, isolating the active material from direct contact with the electrolyte and mitigating undesirable side reactions.[5–7] The second approach involves optimizing the electrolyte composition to enable the *in situ* formation of a stable SEI film by electrochemical methods, including the use of electrolyte additives[8–11] and novel electrolyte systems.[12–16]

To date, substantial efforts have been devoted to exploring strategies to modulate the electrolyte solvation structure to construct a unique SEI structure. It has been acknowledged that the ideal SEI possesses a bilayer structure, characterized by an inorganic inner layer and an organic outer layer, which has been extensively validated in lithium metal and graphite anodes.[17,18] By modulating the type and concentration of the solvent, the formation of the solvation structure can be precisely controlled, thereby influencing the characteristics of the SEI.[19] Specifically, to construct the anion-enriched solvation structure, the double-layer SEI was intentionally constructed.[20–25] Except for electrolyte engineering, electrochemical strategies have also been proven to generate a LiF[26,27] or t-Li$_2$ZrF$_6$-rich[1] interfacial layer without significantly changing the solvation structure, which could markedly accelerate Li-ion transfer and suppress the growth of Li dendrites. However, our recent research[28] has revealed that incorporating oligomer layers to anchor inorganic particles is available to accommodate destructive volume expansion of Si anodes to maintain interphase stability. Despite these advances, the large particle size and non-uniform distribution of inorganic components may still exhibit a large lithium-ion (Li$^+$) diffusion barrier within the SEI.[29–31] In this regard, Wang *et al.* pointed out that downscaling the crystal size of the electrode materials is the essential parameter to diminish the lithiation kinetics.[30] The smaller grain sizes with a larger grain boundary area serve as preferential channels for Li$^+$ migration. Therefore, the reduced diffusion distance and energy barrier of Li$^+$ are conducive to enhancing the diffusion kinetics during the electrochemistry process. Similarly, finer grains have also been shown to contribute to the synergistic effect of high strength and good ductility for most metallic materials to accommodate stress and strain.[32,33] And when applied to lithium-ion batteries (LIBs), the fine-grained cathode and anode materials can effectively enhance the specific surface area, reduce the ion diffusion path, and improve the structural stability.[34,35] How about exploring the ion diffusion kinetics and electrochemical performance by tailoring a fine-grained SEI on the Si surface, an approach that has never been considered?

Herein, a multilayer fine-grained SEI layer was first proposed to be constructed on the Si surface by using a pulse electrochemical activation mode. By precisely regulating the decomposition potentials of individual electrolyte components and the growth time of inorganic species in each layer, the grain size can be controlled and uniformly distributed within the organic matrix of each SEI layer. The fine-grained SEI consists of multiple layers, with small inorganic particles evenly distributed from the inside out, bonded with flexible organic components. Moreover, the multilayer fine-grained SEI offered uniform ionic pathways, thereby obtaining a lower Li$^+$ diffusion barrier, which is only 1/5 of the typical double-layer SEI. Additionally, Young's modulus of the multilayer fine-grained SEI is 12.5 GPa, significantly higher than that of the typical double-layer SEI (5.1 GPa). The strengthened rigidity and flexibility characteristics enhanced the structural stability of the SEI and enabled it to accommodate the huge volume expansion of the Si anode during cycling. The feasibility of this approach has been rigorously examined through both experimental characterization and theoretical analysis, with further studies into the interface properties and Li$^+$ diffusion mechanisms after grain refinement. To be specific, the Si/C anode exhibits excellent capacity retention (84.5%) after 400 cycles at a loading of 3 mg cm^{-2}. Furthermore, the Si/C∥LiFePO$_4$ full battery remains at 93.6% of its capacity after 583 cycles at a current density of 1 A g^{-1}.

Results and discussion

Multilayer fine-grained SEI structure design

The electrochemical performance of Si-based anodes is primarily influenced by both the composition and structure of the SEI. It is generally accepted that the anion-enriched solvation structure is able to generate classical SEI bilayer structures through two-step reduction: the anion reduction at a high plateau (stage ①) and solvent reduction at the low voltage (stage ③) (Fig. 1a).[36,37] While the increased inner bulk inorganic components provide good rigidity, the incompatible organic polymers fail to effectively bind the nonadjacent bulk inorganic material together. This results in low Li$^+$ diffusivity and poor flexibility, which hampers its ability to accommodate the huge volume expansion of the Si anode during long-term cycling.[38] Recently, the additive has been deliberately introduced to participate in an anion solvation sheath to generate low molecular weight oligomers after anion reduction (stage ②) (Fig. 1b).[28] The short-chain structure of oligomers facilitates the binding of bulk inorganic species, making the SEI structure both rigid and flexible. This enables the SEI to better adapt to the volumetric expansion of the Si anode during cycling.

However, the presence of such large inorganic particles will result in low Li$^+$ diffusivity. To address this issue, we hypothesize constructing fine-grained inorganic particles constituting the SEI layer by optimizing the electrochemical activation method. Theoretically, different electrochemical reactions occur under different potential conditions. Thereupon, we deliberately manipulate the growth behavior of inorganic and organic species by controlling the voltage and reaction time during the reduction process (Fig. 1c). To be expected, the resultant multilayer fine-grained SEI exhibits improved rigidity and flexibility, allowing it to better accommodate the significant volumetric expansion of the Si anode during long-term cycling. More importantly, the numerous fine-grained interfaces are beneficial to boost ion diffusion kinetics. A kind of localized high-concentration electrolyte with 10% fluoroethylene carbonate (FEC) and 5% lithium nitrate
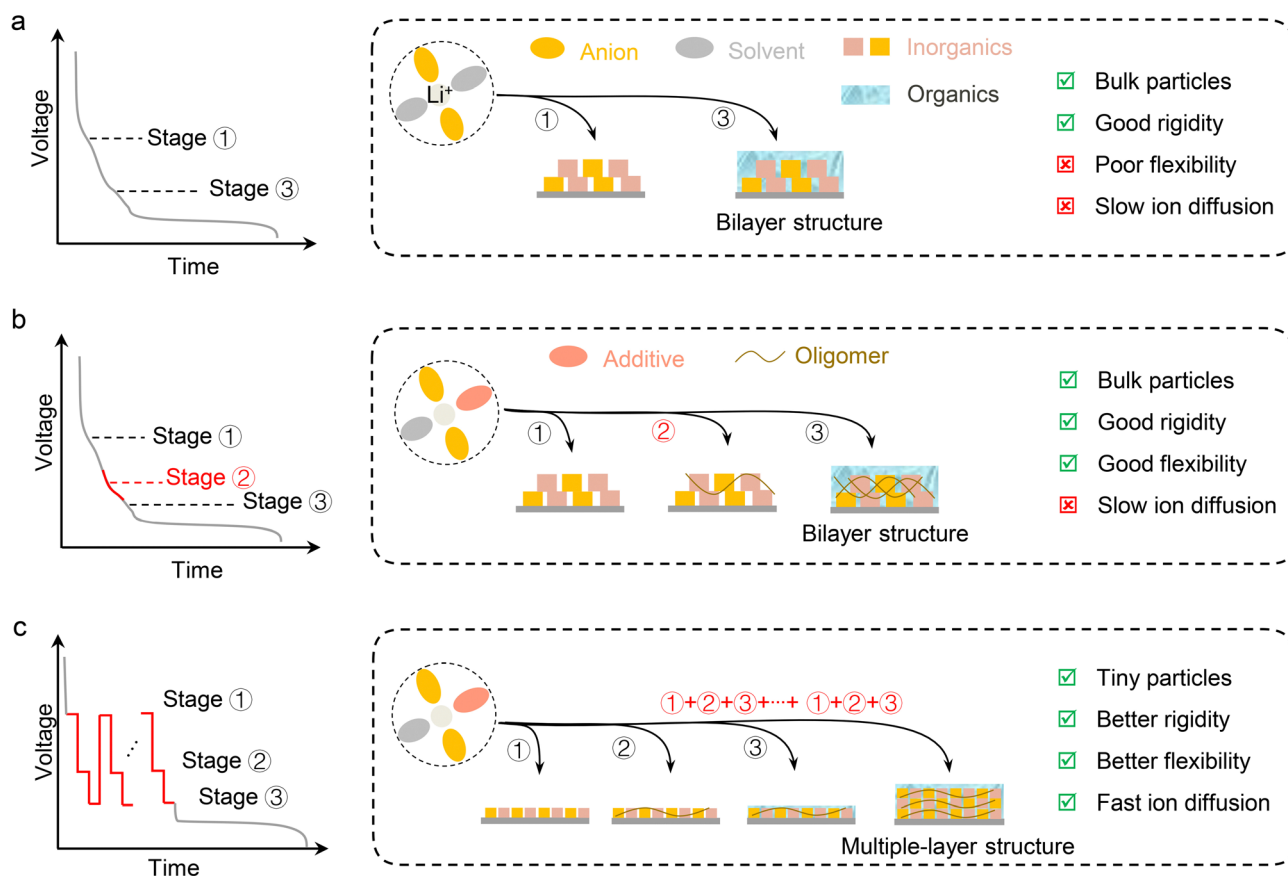
Fig. 1 Different SEI structures constructed by different electrochemical activation methods. (a) SEI formation by linear cyclic voltammetry with an anion-enriched solvation structure; (b) SEI formation by linear cyclic voltammetry with an anion-enriched solvation structure with additives; (c) SEI formation by the pulse voltage intervention with an anion-enriched solvation structure with additives.

(LiNO$_3$) additives (LHCE-FL) has been proven to produce bilayer structures with oligomers with good rigidity and flexibility.[39,40] Herein, LHCE-FL is also used as a proof-of-concept, while the molecular aggregation states and the molecular dynamics snapshots are depicted in Fig. 2a and Fig. S1 (ESI†), respectively. Density functional theory (DFT) calculations are then used to compare the activation energy changes of dimethyl ether (DME), FEC, lithium bis(fluorosulfonyl)imide (LiFSI), and LiNO$_3$, as well as their theoretical decomposition voltages (Fig. 2b and Fig. S2, ESI†). Clearly, the lithium salts, LiNO$_3$ and LiFSI, are the first batch to be reduced to inorganic Li$_3$N and LiF at above 1.4 V, while FEC and DME are prone to generate oligomers and high molecular weight polymers at about 1.1 and 0.8 V, respectively. Then, linear sweep voltammetry (LSV) was conducted on the Si/C anode to ascertain the decomposition voltages of each ingredient. As shown in Fig. 2c, there are three obvious dI/dV peaks, located at 1.28–1.51, 0.90–1.12, and 0.75–0.85 V consistent with the results of LSV (Fig. S3, ESI†), corresponding to different electrochemical reduction processes. To more precisely confirm the optimal decomposition voltages, discharging at a constant voltage is adopted to compare the coulombic efficiency (CE) of the reversible capacity (Fig. 2d). Specifically, it was found that the constant voltages at 1.4, 1.0, and 0.8 V correspond to the highest CE for each respective stage, as shown in Fig. 2e and Fig. S4–S6 (ESI†).

Based on the above results, a pulse constant voltage decomposition experiment was designed, as shown in Fig. 2f. The SEI was constructed at the decomposition voltages of LiNO$_3$/LiFSI (1.4 V), FEC (1.0 V), and DME (0.8 V), respectively, for a short time, and the process was repeated several times to control the grain particle size, which is referred to as "consSEI-xth", where x indicates the number of repeating times. For comparison, the common electrochemical method to construct the SEI layer is referred to as "w/o consSEI". The differences in the initial CE and discharge capacity are obvious with constructing different times, as depicted in Fig. 2g and Fig. S7–S11 (ESI†), where the Si/C electrode with consSEI-100th shows the highest average initial CE and capacity of 86.3% and 1244 mA h g^{-1}, respectively. Furthermore, consSEI-100th maintains the highest specific discharge capacity even after 100 cycles at a current density of 1 A g^{-1} (Fig. 2h).

Morphology and structure analysis of the SEI layer

The unique structure of the multilayer fine-grained SEI on the Si/C anode is then investigated. Cryo-transmission electron microscopy (Cryo-TEM) as shown in Fig. S12 (ESI†) reveals the typical bilayer structure of w/o consSEI, consisting of an inorganic inner layer and an organic outer layer. In comparison, consSEI-xth shows superimposed structures, while the
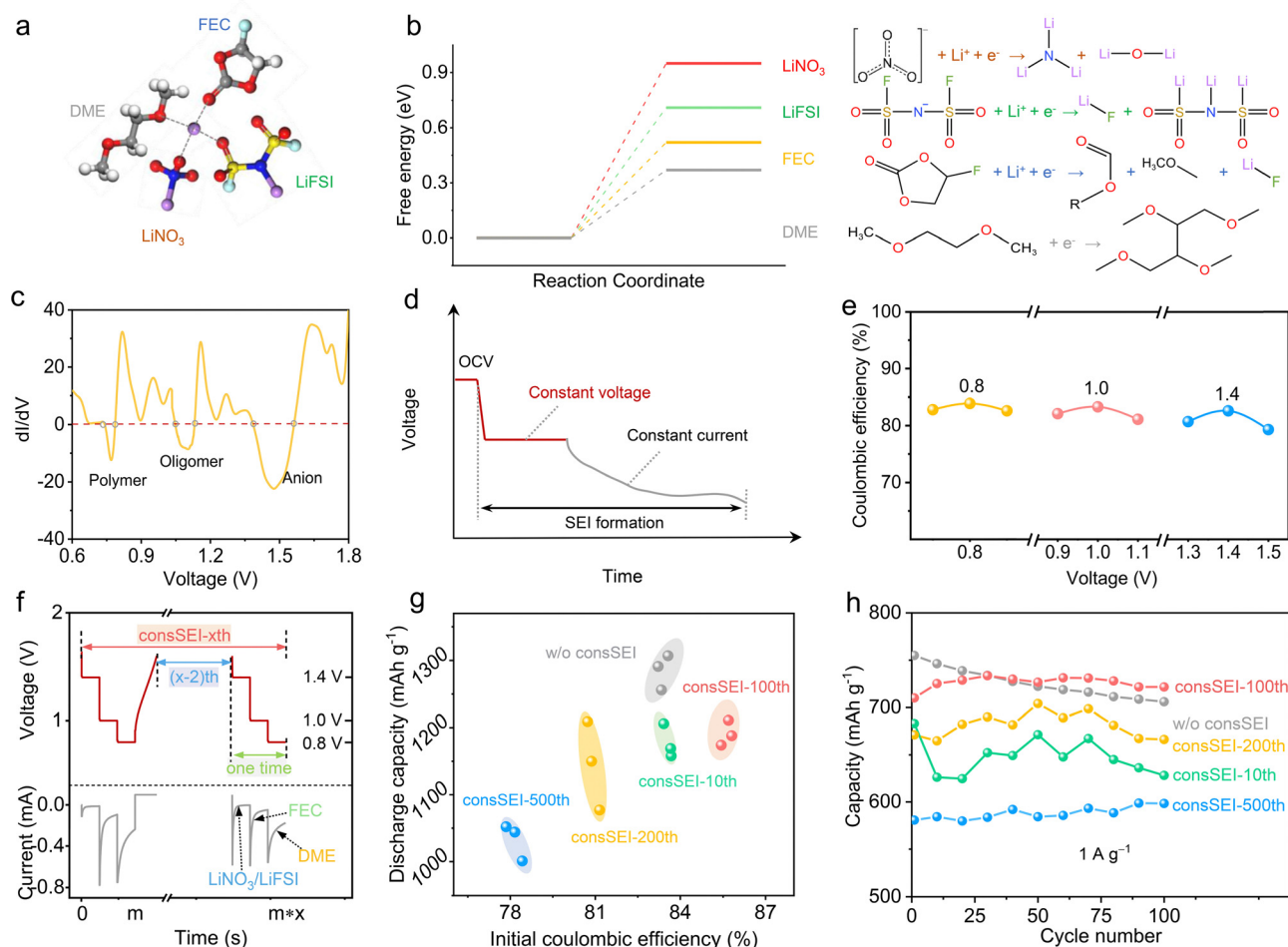
Fig. 2   The design principle for constructing a fine-grained SEI layer. (a) The solvation structure of the LHCE-FL electrolyte based on molecular dynamics simulation; (b) different activation energies for the decomposition of LiNO₃, LiFSI, FEC, DME, and the corresponding decomposition reactions; (c) the derived d*I*/d*V*–voltage curves from LSV; (d) the schematic of constant voltage discharging and the corresponding (e) coulombic efficiency; (f) the schematic of designed pulse constant voltage discharging and the corresponding (g) initial coulombic efficiency and discharge capacities, and (h) long-term cycling performance.

"*x*th" representing repeating times, and the more repeating times corresponding to the more superimposed layers (Fig. 3a and Fig. S13, S14, ESI†). Furthermore, as confirmed by electron diffraction (Fig. 3b and Fig. S13b, ESI†), it is evident that LiNO₃ and LiFSI decompose to form the inorganic components Li₃N and LiF during SEI construction, and these materials are present in each layer of the SEI. As expected, consSEI-100th features a layered structure with small Li₃N and LiF particles present in each SEI layer, as shown in Fig. 3c, while the sample w/o consSEI shows larger inorganic particles in the inner side for comparison (Fig. 3d). This suggests that the pulse electrochemical method of consSEI-100th forms a fine-grained SEI layer with a multilayered structure that is distinct from that formed w/o consSEI.

To further investigate the regulatory effect of consSEI-100th on SEI components at the Si/C anode surface, the interface composition after SEI construction was analyzed using X-ray photoelectron spectroscopy (XPS). Before that, the decomposition products at different voltages are validated. Fig. S15a and d

(ESI†) show that LiNO₃ and LiFSI decompose at 1.4 V, and the highest concentrations of Li₃N and LiF indicate that much organics is produced at this voltage. Sweeping to 1.0 V (Fig. S15b and e, ESI†), the ratios of Li₃N and LiNₓOᵧ of N 1s decrease, while the ratio of LiF barely changes suggesting that some inorganic compounds are also generated during FEC decomposition. Finally, at 0.8 V (Fig. S15c and f, ESI†), where DME decomposes to only produce organic materials, the ratio of LiF in F 1s and that of Li₃N and LiNₓOᵧ in N 1s all decreases.

To further validate our hypothesis regarding the construction of a multilayer fine-grained SEI, we conducted an in-depth analysis of the interphase during the formation process using *ex situ* XPS. And the changes in SEI composition during the voltage transitions in the initial cycle from open-circuit voltage skipping to 1.4 V (Stage 1), then to 1.0 V (Stage 1 to 2), and finally to 0.8 V (Stage 1 to 2 to 3) were analyzed. Fig. S16 (ESI†) presents the normalization data and it shows that with increasing construction stages, the organic is formed so that the content of LiF and Li₃N decreases, indicating that each SEI
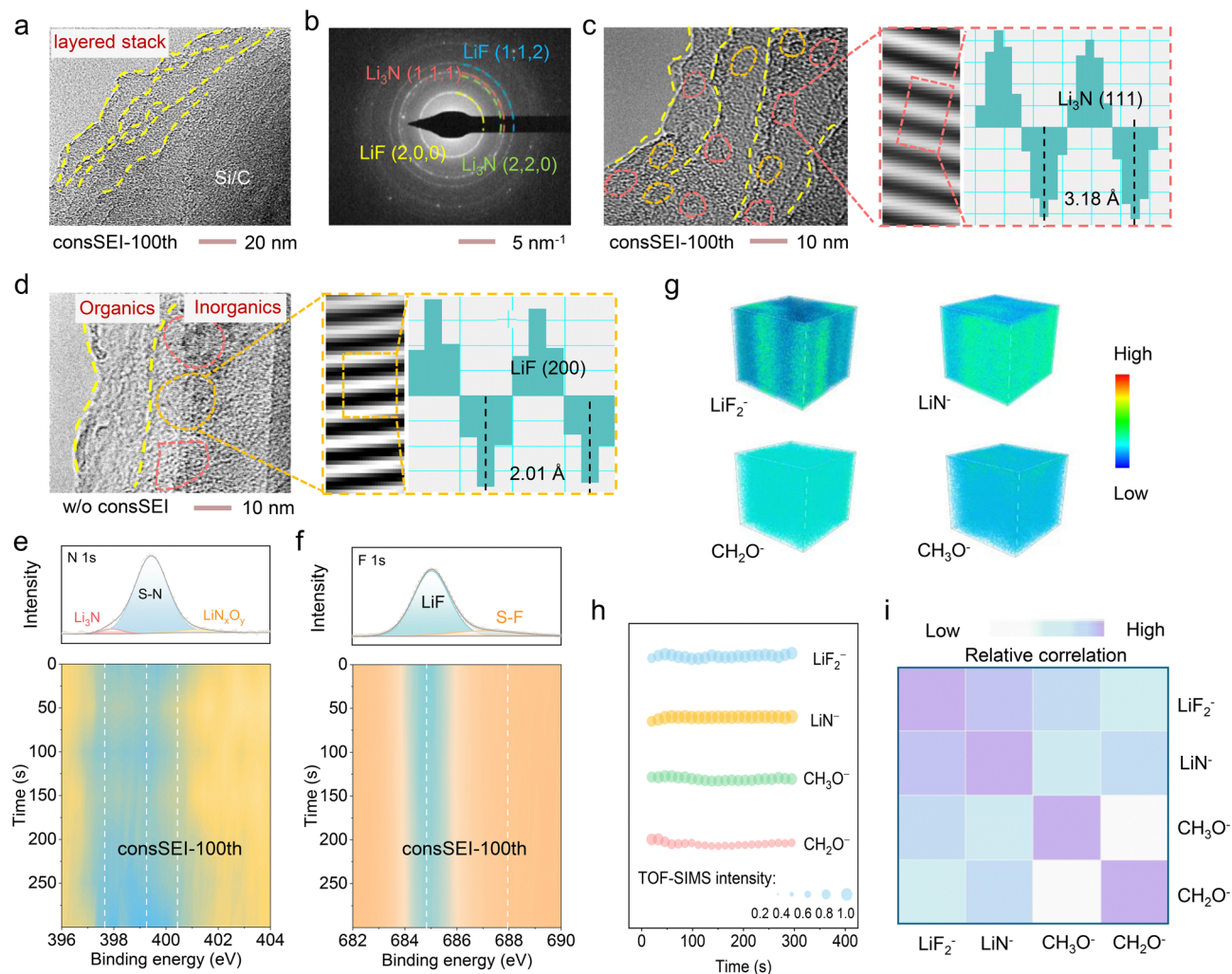
Fig. 3 Morphology and composition analysis of the multilayer fine-grained SEI layer. (a) Cryo-TEM images of the SEI in consSEI-100th; (b) selected-area electron diffraction of the SEI in consSEI-100th; magnified HRTEM images and the corresponding FFT images of the SEI in (c) consSEI-100th (d) w/o consSEI; depth sputtering (e) N 1s and (f) F 1s XPS contour plots of the Si/C anode after cycling in consSEI-100th; (g) 3D TOF-SIMS sputtering images and the selected secondary ion fragments (LiF_2^-, LiN^-, CH_2O^- and CH_3O^-) of the cycled Si/C anode in consSEI-100th and the corresponding (h) normalized (to maximum) TOF-SIMS depth profiles of characteristic fragments; (i) relative correlation matrix for the fragments of interest (LiF_2^-, LiN^-, CH_2O^- and CH_3O^-).
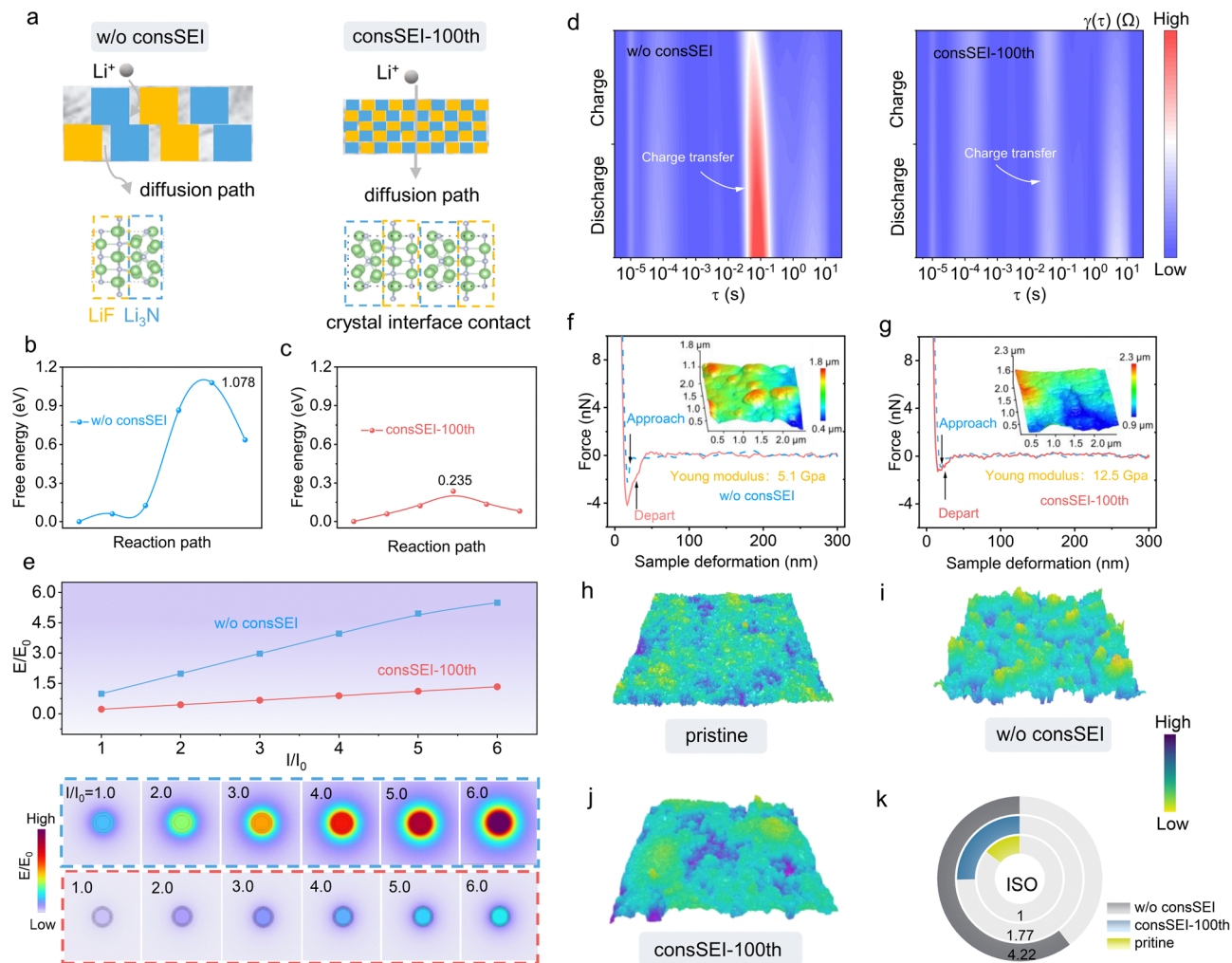
layer is composed of inorganics wrapped in organics. Additionally, the SEI structure of consSEI-100th was analyzed by XPS and Ar$^+$ sputtering depth profiling. Fig. 3e and f demonstrate that with increasing Ar$^+$ sputtering time, the organic and inorganic components of the SEI remain almost consistent, indicating uniform distribution across each SEI layer. Time-of-flight secondary ion mass spectrometry (TOF-SIMS) also indicates the uniform spatial distribution of the different SEI components. The three-dimensional images in Fig. 3g, along with Fig. S17 and Fig. 3h (ESI†), show little variation in the spatial distribution of inorganic LiF_2^-, LiN^-, and organic fragments such as CH_2O^- and CH_3O^-. This indicates that the oligomers derived from FEC and the organic components produced by DME decomposition are uniformly within the SEI, interwoven with the inorganic Li_3N and LiF to form a stable and intertwined structure.[23,41]

Furthermore, Fig. 3i illustrates the close correlation between the inorganic LiF_2^-, LiN^-, and organic fragments (CH_2O^- and

CH_3O^-) in the SEI layer. This phenomenon can be attributed to the formation of the multilayer fine-grained SEI, wherein the smaller grain size facilitates an increased number of reaction sites. Consequently, the composition within each layer of the SEI is more uniformly distributed, leading to stronger correlations among individual components.

Advantages of the multilayer fine-grained SEI layer

Theoretically, the SEI with inorganic particles of varying sizes significantly influences the ion diffusion kinetics. As the grain size is refined to create a higher number of grain boundaries, the diffusion path is significantly shortened, allowing Li$^+$ to move more easily through the SEI (Fig. 4a), which is beneficial to enhance the rate capability. Then, to investigate the mechanism behind the multilayer fine-grained SEI layer of consSEI-100th, the Li$^+$ diffusion energy barrier for both w/o consSEI and consSEI-100th was calculated using first principles. Due to the increased grain boundary contact between Li_3N and LiF in

7064 | *Energy Environ. Sci.*, 2025, **18**, 7060–7070

This journal is © The Royal Society of Chemistry 2025

Fig. 4 Dynamic performance and interphase characterization. (a) Schematic diagram of Li$^+$ diffusion in the fine-grained SEI layer; Gibbs free energy of the Li$^+$ diffusion path in the sample (b) w/o consSEI and (c) consSEI-100th model; (d) DRT impedance spectra of the Si/C electrode with consSEI-100th and w/o consSEI; (e) the electric field intensity distribution, the changes of the maximum electric field intensity for samples w/o consSEI and with consSEI-100th at different current densities; the effects of stress engineering by COMSOL modeling; quantitative nanomechanical mapping of the cycled Si/C anode (f) w/o consSEI and (g) with consSEI-100th, with insets showing the corresponding AFM morphologies; spectral diagram of the 3d profiler: (h) pristine, (i) w/o consSEI, (j) consSEI-100th, and corresponding (k) roughness.

consSEI-100th (Fig. S18, ESI†), the energy barrier is 0.235 eV for consSEI-100th as illustrated in Fig. 4c, which is much lower than that for w/o consSEI as shown in Fig. 4b (1.078 eV). The lower diffusion energy barrier in consSEI-100th indicates more efficient ion transportation. To verify this, *in situ* electrochemical impedance spectroscopy (EIS) was used to analyze the charge transfer kinetics (Fig. S19, ESI†). By converting the EIS data into a relaxation time distribution function in the time domain, a continuous curve with distinct peaks, where each one corresponds to a specific dynamic process, can be obtained. As shown in Fig. S20 (ESI†), the peak around 10^{-5}–10^{-3} s corresponds to the ohmic internal resistance (R_{ob}), while those at 10^{-3}–10^{-2} s and 10^{-2}–10^{-1} s correspond to the ohmic impedance (R_{SEI}) and the charge transfer impedance (R_{ct}).[42] Clearly in Fig. 4d, the R_{ct} during the whole Si/C alloying and dealloying reaction for w/o consSEI is consistently higher than that for consSEI-100th. Furthermore, the diffusion behavior of

Li$^+$ in different Si/C electrodes was compared by using a galvanostatic intermittent titration technique (GITT), and the Li$^+$ diffusion coefficient (D_{Li^+}) was calculated using eqn (1):[43–47]

$$D_{Li^+} = \frac{4}{\pi\tau}\left(\frac{n_M V_M}{S}\right)^2\left(\frac{\Delta E_s}{\Delta E_\tau}\right)^2 \qquad (1)$$

where τ = 3600 s, n_M and V_M are the molar amount and molar volume of Si/C, respectively, and the electrode area is 1.13 cm^2. As depicted in Fig. S21 (ESI†), the calculated average D_{Li^+} for consSEI-100th during lithiation and de-lithiation is 4.53 × 10^{-10} cm^2 s^{-1}, an order of magnitude higher than that for w/o consSEI (5.51 × 10^{-11} cm^2 s^{-1}). These results indicate that the multilayer fine-grained SEI is beneficial in reducing interfacial and charge transfer resistances, leading to enhanced electrochemical performance.

This journal is © The Royal Society of Chemistry 2025

Energy Environ. Sci., 2025, **18**, 7060–7070 | **7065**

To further examine the effect of SEI grain refinement on the stress and strain of the Si/C anode, finite element simulations were performed using COMSOL Multiphysics. The variations in current (I/I_0) and electric field intensity (E/E_0) were introduced to assess the stress and strain of the Si/C anode.[48,49] Fig. S22 (ESI†) shows enlarged images of the original states for both w/o consSEI and consSEI-100th, where it is evident that the SEI structure on the surface of Si/C particles in consSEI-100th is more refined. As illustrated in Fig. 4e, the simulated electric field intensities increase with the increasing current. Compared to consSEI-100th, the electric field strength for the sample w/o consSEI is always more pronounced with increasing current, hinting at the enhanced stress and strain in the Si/C electrode that lead to severe structural damage and failure during repeated cycling.[50] This indicates that the consSEI-100th feature of the multilayer fine-grained SEI structure is more rigid and flexible, enabling it to better accommodate the volume expansion of the Si/C anode caused by Li–Si alloying/de-alloying behavior. To further explore the impact of the multilayer fine-grained SEI on the physical properties of the Si/C anode surface, atomic force microscopy (AFM) was employed. As shown in Fig. 4f and g, the surface Young's modulus of the Si/C anode with consSEI-100th is 12.5 GPa, significantly higher than that of the sample w/o consSEI (5.1 GPa). Moreover, comparing the morphology of the original state of the Si/C anode (Fig. S23, ESI†) and high-resolution AFM images (Fig. S24, ESI†), the morphology development of consSEI-100th is minimal in comparison with that of the sample w/o consSEI. Finally, to investigate the overall state of the Si/C anode after SEI construction, 3D optical profilometry was also used. Fig. S25 (ESI†) shows that during SEI construction, the electrode surface becomes flatter as the SEI construction progresses, indicating that the formation of organics with flexible properties gradually increases during the SEI construction process and provides the electrode with some flexibility and smoothness. Furthermore, Fig. 4h–j and Fig. S26 (ESI†) demonstrate that after cycling, the pole pieces of consSEI-100th are more uniform compared to those of the counterparts. To further quantify the flatness, Fig. 4k calculates that the roughness of the consSEI-100th electrode is reduced to 1.77 far, significantly lower than that of the sample w/o consSEI (4.22), indicating smoother characteristics. Therefore, it demonstrates that the multilayer fine-grained SEI possesses both excellent flexibility and rigidity, making it more adaptable to the significant volume expansion of the Si/C anode during the cycling process.
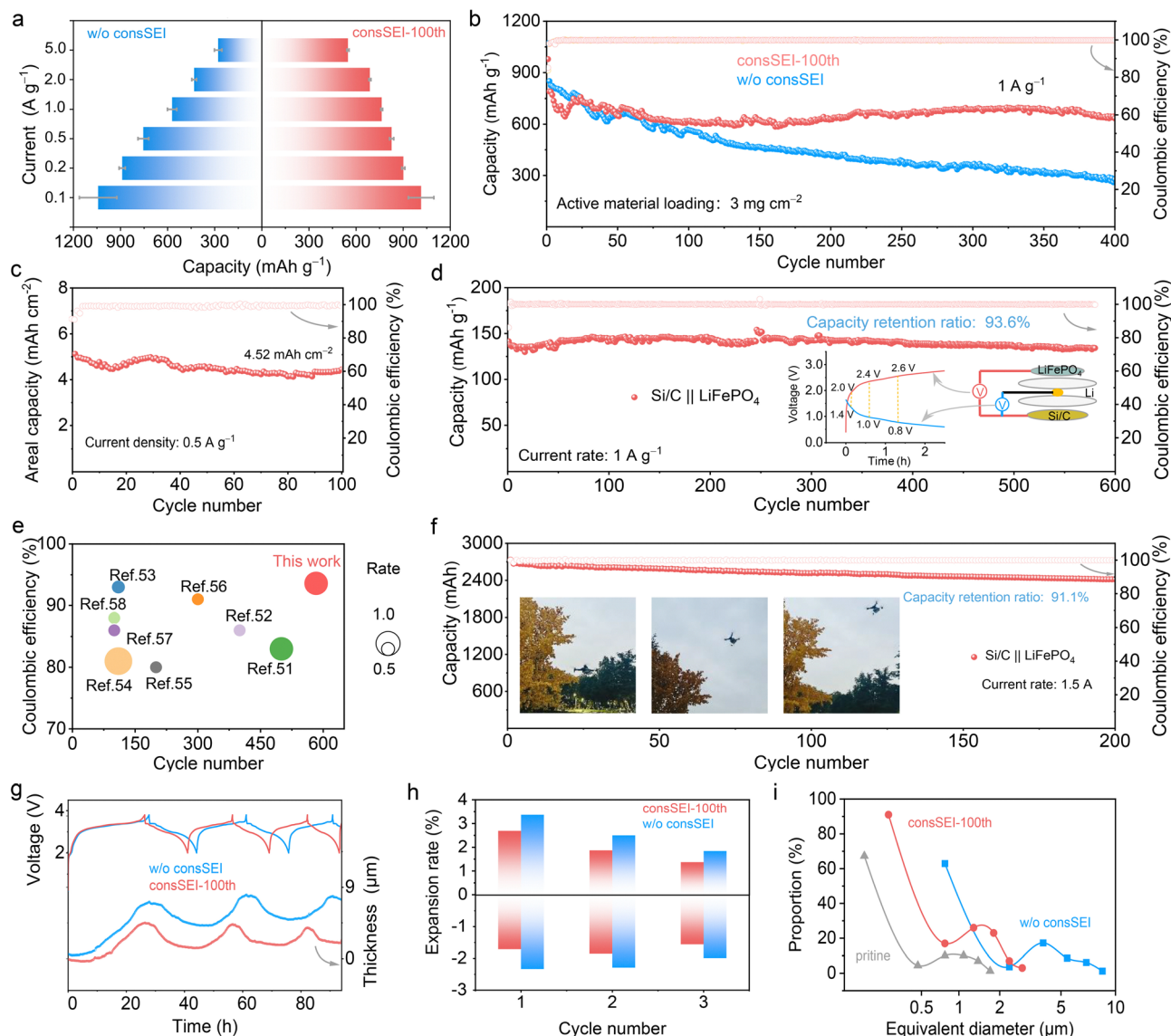
Electrochemical performances

To verify the potential of *in situ* construction of multilayer fine-grained SEI layers for practical LIBs, the electrochemical properties of the Si/C anode were investigated. First, Li∥Si/C half cells were prepared. Fig. S27 (ESI†) shows the initial charge and discharge curves at a current density of 0.1 A g^{-1}. As expected, the Si/C anode of consSEI-100th shows a lower initial discharge capacity of 1256 mA h g^{-1}, compared with that of the sample w/o consSEI ($\sim$1321 mA h g^{-1}), which can be attributed to the construction of the SEI before battery testing. Then, the rate

capabilities at various current densities of the Si/C anode with different SEI layers were compared. As shown in Fig. 5a, Si/C anodes with different SEIs exhibit comparable discharge capacities at low current densities (0.1–0.5 A g^{-1}). However, with the increasing current density, the Si/C electrode with consSEI-100th shows the obviously enhanced specific capacity compared with the counterpart. Specifically, the Si/C anode with consSEI-100th could deliver a reversible capacity as high as 567 mA h g^{-1} even at 5 A g^{-1}, which is far beyond the sample w/o consSEI (278 mA h g^{-1}). Their difference in rate performance obviously hints that consSEI-100th could remarkably enhance the Li–Si electrochemistry kinetics. Fig. 5b then compares the long-cycling performance of the Si/C anode with different SEI layers at a mass loading of 3 mg cm^{-2}. After 400 cycles at a current density of 1 A g^{-1}, the Si/C anode of consSEI-100th exhibits an excellent capacity of 645 mA h g^{-1}, accompanied by a good capacity retention as high as 84.5%. As for the Si/C anode w/o consSEI, it only delivers an inferior capacity of 283 mA h g^{-1} with a low retention of 44.3%. This is logically attributed to the enhanced mechanical strength of consSEI-100th, which not only effectively mitigates the volume expansion of Si/C particles but also guarantees the structural integrity of the entire electrode during cycling. Moreover, the Si/C anode with consSEI-100th could afford an area capacity of 4.52 mA h cm^{-2} at 0.5 A g^{-1} with stable cycling for 100 cycles (Fig. 5c), highlighting the high reversibility of the Li–Si alloy/dealloying behavior.

To further assess the practical applicability of consSEI-100th, commercial zero strain LiFePO$_4$ cathodes and Si/C anodes were assembled into full batteries, and the performance of the coin cell was first tested. Prior to assembling the Si/C∥LiFePO$_4$ cell, the practical potential for constructing the multilayer fine-grained SEI was determined by a self-made three-electrode (Si/C–Li–LiFePO$_4$) setup (Fig. S28, ESI†). As shown in the inset of Fig. 5d, the pulse voltages for constructing multilayer fine-grained SEI layers are 2.0, 2.4, and 2.6 V, respectively, corresponding to 1.4, 1.0, and 0.8 V in the half cell. After constructing the SEI 100 times (Fig. S29, ESI†), the Si/C∥LiFePO$_4$ full battery was then subjected to cycling. Fig. S30 (ESI†) shows the initial charge and discharge curve at 0.1 A g^{-1} with an initial CE of 96.2%. The long-term cycling performance of the Si/C∥LiFePO$_4$ coin cell at a current density of 1 A g^{-1} is presented in Fig. 5d. As shown, the full cell delivers an ultra-stable cycling capability with a capacity retention of 93.6% after 583 cycles, while the coinciding charge and discharge curves at different cycle numbers without apparent voltage polarization and capacity decay as shown in Fig. S31 (ESI†) suggest good reversibility of the electrochemical reaction. In comparison with the other recent studies on Si/C anodes,[51–58] the cycling capability presented in this work demonstrates obvious superiority (Fig. 5e and Table S1, ESI†).

Encouraged by the impressive performance of the Si/C∥LiFePO$_4$ coin-cell, a commercial Si/C∥LiFePO$_4$ pouch cell (about 3.0 A h) was used to further evaluate the practical potential of the multilayer fine-grained SEI. Fig. S32 (ESI†) shows the structural diagram of the Si/C∥LiFePO$_4$ pouch cell.

7066 | *Energy Environ. Sci.*, 2025, **18**, 7060–7070

This journal is © The Royal Society of Chemistry 2025

Fig. 5 Electrochemical performances of Si/C anodes with different SEI layers. (a) Comparison of the rate capabilities of the Si/C anode with different SEI layers; (b) cycling stabilities of the Si/C anode with the mass loading of 3 mg cm^{-2} at 1 A g^{-1}; (c) cycling performance of the Si/C electrode with consSEI-100th at 0.5 A g^{-1}; (d) long-term cycling stability of the Si/C electrode with consSEI-100th in the Si/C∥LiFePO$_4$ coin-cell and (e) in comparison with previous works, the inset in (d) gives the three-electrode profile of the Si/C∥LiFePO$_4$ full cells; (f) cycling capability of the Si/C∥LiFePO$_4$ pouch cell in consSEI-100th, and the insets show the picture of this Si/C∥LiFePO$_4$ pouch cell in drone application; (g) thickness variation of the Si/C electrode during the charging and discharging process and the corresponding (h) volume expansion rate; (i) comparison of particle size of the Si/C composites before and after cycling.

As observed, the Si/C∥LiFePO$_4$ pouch cell achieves an initial CE of up to 94% at 0.1 A current (Fig. S33, ESI†). At a current density of 1.5 A, the reversible capacity of the Si/C∥LiFePO$_4$ pouch cell remains at 2.47 Ah even after 200 cycles, corresponding to the capacity retention of 91.1% (Fig. 5f). By viewing the charge and discharge curves of the Si/C∥LiFePO$_4$ pouch cell, as shown in Fig. S34 (ESI†), it only shows a slight capacity decay without severe voltage drop after prolonging the cycle number, confirming the excellent unmanned aircraft practical potential of this SEI tailoring strategy in high-energy LIBs (the inset pictures of Fig. 5f). Furthermore, it demonstrates that the fine-grained SEI achieved by consSEI-100th exhibits a more uniform structure, thereby reducing interfacial charge transport resistance, enhancing Li$^+$ diffusion kinetics, and contributing to improved rate performance and energy efficiency of the battery. Additionally, this SEI possesses both rigidity and flexibility, enabling it to accommodate volume changes in electrode materials during charging and discharging processes, thus preventing SEI rupture and spalling.

To explore the in-depth reason for the cycling stability of the Si/C anode with consSEI-100th in half and full cells, an *in situ* electrode thickness monitoring and postmortem SEM analysis were carried out to investigate the structure variation of electrodes and materials. Fig. 5g records the thickness–time curves

This journal is © The Royal Society of Chemistry 2025

Energy Environ. Sci., 2025, **18**, 7060–7070 | **7067**

of the Si/C electrode w/o consSEI and with consSEI-100th in the Si/C∥LiFePO$_4$ coin cell during charge and discharge. Clearly, the cell with consSEI-100th shows a smaller thickness expansion compared with that w/o consSEI. By calculation, it is found that the thickness expansion/shrinkage ratios of the Si/C electrode with consSEI-100th are 2.6%/1.7%, 1.8%/1.8%, and 1.3%/1.5% in the first three cycles (Fig. 5h). However, for the Si/C electrode w/o consSEI, the thickness expansion/shrinkage ratios are significantly enhanced. This thickness variation can also be observed by the postmortem cross-sectional SEM images (Fig. S35, ESI†) and *in situ* optical images (Fig. S36 and S37, ESI†) of the cycled Si/C electrode. Furthermore, the surface morphology of the electrode was analyzed by SEM and *in situ* optical imaging reveals that the thickness of consSEI-100th varies less, which indicates that consSEI-100th can maintain particle stability and constrain the volume expansion of Si/C particles after cycling. Moreover, Fig. S38 (ESI†) provides the postmortem SEM images of the three Si/C electrodes, while Fig. 5i gives the statistical result of the Si/C particles. Although the grain size of the Si/C anode in the consSEI-100th and w/o consSEI electrode shows obvious augmented compared to the pristine sample, the grain size in the consSEI-100th electrode after cycling is obviously lower than that in the sample w/o consSEI. This result indicates that the fine-grained SEI structure in the consSEI-100th electrode with the characteristics of uniformity, rigidity, and flexibility can effectively accommodate the volume expansion of Si/C particles, which is in favor of avoiding the repeated construction of the SEI layer and electrolyte deterioration, eventually ensuring the long-term cycling stability and lifespan of the Si-based electrode.

Conclusions

In conclusion, we presented a pulse electrochemical activation maneuver to form a multilayer fine-grained SEI structure on the Si/C anode. This approach ensures a uniform distribution of tiny inorganic particles (LiF/Li$_3$N) and an interwoven organic buffer layer, resulting in a rigid yet flexible multi-layered SEI. As a result, this multilayer fine-grained SEI is able to accommodate the huge volume expansion of the Si-based anode during cycling, thereby maintaining the integrity of both the electrode sheet and particles. Comprehensive characterization demonstrates the viability of our strategy, while DFT calculations reveal a reduced Li$^+$ diffusion energy barrier after grain refinement. Furthermore, mechanical analysis confirms that the improved rigid-flexible SEI structure effectively accommodates the Si anode's volume changes. Consequently, the multilayer fine-grained SEI maintains a very stable interphase and the Si-based anode exhibits excellent capacity retention (84.5%) after 400 cycles at a current density of 1 A g^{-1}. Furthermore, the Si/C∥LiFePO$_4$ full battery retains 93.6% of its capacity after 583 cycles at a current density of 1 A g^{-1}. This work sheds valuable insights into the design of SEI structures for high-volume expansion electrode materials in high-energy secondary ion batteries.

Author contributions

Y. Zhang and W. Cai conceived and designed the experiments. C. Xu prepared the materials and conducted the characterization of materials and batteries. F. Wu, X. Liu, Q. Liu, Y. Jia, X. Zhang, K. Wu, and Z. Song helped to synthesize materials. P. Xia, J. Peng, and Q. He helped to analyze materials. P. Jing designed the toy devices for the pouch cell powering demonstration. C. Xu wrote the manuscript. W. Cai edited the manuscript. All authors discussed the results and have given approval to the final version of the manuscript.

Data availability

The datasets used and analyzed during the current study are available from the corresponding author upon reasonable request.

Conflicts of interest

There are no conflicts to declare.

Acknowledgements

References

1 Y.-F. Tian, S.-J. Tan, C. Yang, Y.-M. Zhao, D.-X. Xu, Z.-Y. Lu, G. Li, J.-Y. Li, X.-S. Zhang, C.-H. Zhang, J. Tang, Y. Zhao, F. Wang, R. Wen, Q. Xu and Y.-G. Guo, *Nat. Commun.*, 2023, **14**, 7247.

2 Q. Xu, T. Li, Z. Ju, G. Chen, D. Ye, G. I. N. Waterhouse, Y. Lu, X. Lai, G. Zhou, L. Guo, K. Yan, X. Tao, H. Li and Y. Qiu, *Nature*, 2025, **637**, 339–346.

3 J. Wang and Y. Cui, *Nat. Energy*, 2020, **5**, 361–362.

4 Q. Liu, X. Wei, C. Yang, C. Xu, W. Cai and F. Chen, *Small*, 2024, **20**, 2403938.

5 Y. Cheng, Z. Wang, J. Chen, Y. Chen, X. Ke, D. Wu, Q. Zhang, Y. Zhu, X. Yang, M. Gu, Z. Guo and Z. Shi, *Angew. Chem., Int. Ed.*, 2023, **62**, e202305723.

6 J. Sun, S. Zhang, J. Li, B. Xie, J. Ma, S. Dong and G. Cui, *Adv. Mater.*, 2023, **35**, 2209404.

7068 | *Energy Environ. Sci.*, 2025, **18**, 7060–7070

This journal is © The Royal Society of Chemistry 2025

7 M. Qin, Z. Zeng, Q. Wu, H. Yan, M. Liu, Y. Wu, H. Zhang, S. Lei, S. Cheng and J. Xie, *Energy Environ. Sci.*, 2023, **16**, 546–556.

8 H. Wang, S. Chen, Y. Li, Y. Liu, Q. Jing, X. Liu, Z. Liu and X. Zhang, *Adv. Energy Mater.*, 2021, **11**, 2101057.

9 J. Tan, J. Matz, P. Dong, J. Shen and M. Ye, *Adv. Energy Mater.*, 2021, **11**, 2100046.

10 Y. Ou, W. Hou, D. Zhu, C. Li, P. Zhou, X. Song, Y. Xia, Y. Lu, S. Yan, H. Zhou, Q. Cao, H. Zhou, H. Liu, X. Ma, Z. Liu, H. Xu and K. Liu, *Energy Environ. Sci.*, 2025, **18**, 1464–1476.

11 H. Wang, J. Liu, J. He, S. Qi, M. Wu, F. Li, J. Huang, Y. Huang and J. Ma, *eScience*, 2022, **2**, 557–565.

12 Y. Liu, Z. Jin, Z. Liu, H. Xu, F. Sun, X.-Q. Zhang, T. Chen and C. Wang, *Angew. Chem., Int. Ed.*, 2024, **63**, e202405802.

13 L. Liu, Z. Shadike, N. Wang, Y.-M. Chen and J.-L. Zhang, *eScience*, 2024, **4**, 100268.

14 X. Zhang, Z. Deng, C. Xu, Y. Deng, Y. Jia, H. Luo, H. Wu, W. Cai and Y. Zhang, *Adv. Energy Mater.*, 2023, **13**, 2302749.

15 Y.-Z. Li, *Science*, 2017, **358**, 506–510.

16 L.-X. Ma, T.-D. Chen, C.-X. Hai, S.-D. Dong, X. He, Q. Xu, H. Feng, A. Xin, J.-T. Chen and Y. Zhou, *Tungsten*, 2024, **6**, 259–268.

17 Z. Deng, Y. Jia, Y. Deng, C. Xu, X. Zhang, Q. He, J. Peng, H. Wu and W. Cai, *J. Energy Chem.*, 2024, **96**, 282–290.

18 W. Cai, Y. Deng, Z. Deng, Y. Jia, Z. Li, X. Zhang, C. Xu, X.-Q. Zhang, Y. Zhang and Q. Zhang, *Adv. Energy Mater.*, 2023, **13**, 2301396.

19 Y. Quan, X. Cui, L. Hu, Y. Kong, X. Zhang, H. Liang, Y. Zhu, C. Wang, N. Zhang and S. Li, *Carbon Neutral*, 2024, **4**, e184.

20 Y. Ko, J. Bae, G. Chen, M. A. Baird, J. Yan, L. Klivansky, D.-M. Kim, S. E. Trask, M.-T. F. Rodrigues, G. M. Carroll, N. R. Neale and B. A. Helms, *ACS Energy Lett.*, 2024, **9**, 3448–3455.

21 W. Zhang, M. Dong, K. Jiang, D. Yang, X. Tan, S. Zhai, R. Feng, N. Chen, G. King, H. Zhang, H. Zeng, H. Li, M. Antonietti and Z. Li, *Nat. Commun.*, 2022, **13**, 5348.

22 N. Wu, J. Shen, X. Zhou, S. Li, J. Li, G. Liu, D. Guo, W. Deng, C. Yuan, X. Liu and H. Hou, *Adv. Energy Mater.*, 2025, **1**, 2405729.

23 B. Jin, A. Dolocan, C. Liu, Z. Cui and A. Manthiram, *Angew. Chem., Int. Ed.*, 2024, **63**, e202408021.

24 B. Jagger and M. Pasta, *Joule*, 2023, **7**, 2228–2244.

25 G.-X. Lu, Q.-Q. Qiao, M.-T. Zhang, J.-S. Zhang, S. Li, C.-B. Jin and Z. J. Hua, *Sci. Adv.*, 2024, **10**, 7348.

26 P. Bai, X. Ji, J. Zhang, W. Zhang, S. Hou, H. Su, M. Li, T. Deng, L. Cao, S. Liu, X. He, Y. Xu and C. Wang, *Angew. Chem., Int. Ed.*, 2022, **61**, e202202731.

27 T. Ma, Y. Ni, Q. Wang, W. Zhang, S. Jin, S. Zheng, X. Yang, Y. Hou, Z. Tao and J. Chen, *Angew. Chem., Int. Ed.*, 2022, **61**, e202207927.

28 C. Xu, P. Jing, Z. Deng, Q. Liu, Y. Jia, X. Zhang, Y. Deng, Y. Zhang and W. Cai, *Energy Storage Mater.*, 2025, **74**, 103911.

29 Y. Luo, J. V. Handy, T. Das, J. D. Ponis, R. Albers, Y.-H. Chiang, M. Pharr, B. J. Schultz, L. Gobbato, D. C. Brown, S. Chakraborty and S. Banerjee, *Nat. Mater.*, 2024, **23**, 960–968.

30 R. Wang, L. Wang, R. Liu, X. Li, Y. Wu and F. Ran, *ACS Nano*, 2024, **18**, 2611.

31 X. Wang, A. Yu, T. Jiang, S. Yuan, Q. Fan and Q. Xu, *Adv. Mater.*, 2024, **36**, 2410482.

32 F. Xing, S. Liao, J. Qin, G. Wang, S. Zheng and Z.-S. Wu, *ACS Energy Lett.*, 2024, **9**, 355–362.

33 S. Mao, Z. Shen, W. Zhang, Q. Wu, Z. Wang and Y. Lu, *Adv. Sci.*, 2022, **9**, 2104841.

34 C. Guo, G. Dai, J. Niu, Y. Guo, Z. Sun, H. Chang and Q. Zhang, *J. Mater. Res. Technol.*, 2023, **26**, 5860–5872.

35 W.-H. C. Y.-Q. Yan, S. Liu, Y. Ma, J.-H. Luan, Z. Rao, C. Liu, Z.-W. Shan, J. Lu and G. Wu, *Science*, 2025, **387**, 401–406.

36 H. Wan, J. Xu and C. Wang, *Nat. Rev. Chem.*, 2024, **8**, 30–44.

37 Q.-K. Zhang, X.-Q. Zhang, J. Wan, N. Yao, T.-L. Song, J. Xie, L.-P. Hou, M.-Y. Zhou, X. Chen, B.-Q. Li, R. Wen, H.-J. Peng, Q. Zhang and J.-Q. Huang, *Nat. Energy*, 2023, **8**, 725–735.

38 L. Wang, J. Yu, S. Li, F. Xi, W. Ma, K. Wei, J. Lu, Z. Tong, B. Liu and B. Luo, *Energy Storage Mater.*, 2024, **66**, 103243.

39 S. Yang, T. Meng, Z. Wang and X. Hu, *Energy Storage Mater.*, 2024, **65**, 103177.

40 Y. Jin, N.-J. H. Kneusels, L. E. Marbella, E. Castillo-Martínez, P. C. M. M. Magusin, R. S. Weatherup, E. Jónsson, T. Liu, S. Paul and C. P. Grey, *J. Am. Chem. Soc.*, 2018, **140**, 9854–9867.

41 Z. He, H. Tu, G. Sun, A. Sun, Y. Wang, J. Sun, G. Wu, W. Li, J. Xu and M. Liu, *Adv. Funct. Mater.*, 2024, **35**, 2414569.

42 J. Tang, Y. Zhou, X. Li, X. Huang, W. Tang and B. Tian, *Energy Mater.*, 2024, **4**, 400022.

43 Z.-X. Chen, Q. Cheng, X.-Y. Li, Z. Li, Y.-W. Song, F. Sun, M. Zhao, X.-Q. Zhang, B.-Q. Li and J.-Q. Huang, *J. Am. Chem. Soc.*, 2023, **145**, 16449–16457.

44 Y.-C. Chien, H. Liu, A. S. Menon, W. R. Brant, D. Brandell and M. J. Lacey, *Nat. Commun.*, 2023, **14**, 2289.

45 Y. Peng, M. Ding, K. Zhang, H. Zhang, Y. Hu, Y. Lin, W. Hu, Y. Liao, S. Tang, J. Liang, Y. Wei, Z. Gong, Y. Jin and Y. Yang, *ACS Energy Lett.*, 2024, **9**, 6022–6028.

46 Y. Peng, C. Zhong, M. Ding, H. Zhang, Y. Jin, Y. Hu, Y. Liao, L. Yang, S. Wang, X. Yin, J. Liang, Y. Wei, J. Chen, J. Yan, X. Wang, Z. Gong and Y. Yang, *Adv. Funct. Mater.*, 2024, **34**, 2404495.

47 W. Wang, F. Xiong, S. Zhu, J. Chen, J. Xie and Q. An, *eScience*, 2022, **2**, 278–294.

48 C. Wang, G. Li, H. Qin, Z. Xiao, D. Wang, B. Zhang, X. Ou and Y. Wu, *Adv. Energy Mater.*, 2022, **12**, 2200403.

49 Q. Li, J. Ruan, S. Weng, X. Zhang, J. Hu, H. Li, D. Sun, X. Wang, F. Fang and F. Wang, *Angew. Chem., Int. Ed.*, 2023, **62**, e202310297.

50 L. Ye, M. Liao, H. Sun, Y. Yang, C. Tang, Y. Zhao, L. Wang, Y. Xu, L. Zhang, B. Wang, F. Xu, X. Sun, Y. Zhang, H. Dai, P. G. Bruce and H. Peng, *Angew. Chem., Int. Ed.*, 2019, **58**, 2437–2442.

51 S. Chen, L. Shen, P. A. van Aken, J. Maier and Y. Yu, *Adv. Mater.*, 2017, **29**, 1605650.

52 W. Wu, Y. Kang, M. Wang, D. Xu, J. Wang, Y. Cao, C. Wang and Y. Deng, *J. Power Sources*, 2020, **464**, 228244.

53 Q. Wang, T. Meng, Y. Li, J. Yang, B. Huang, S. Ou, C. Meng, S. Zhang and Y. Tong, *Energy Storage Mater.*, 2021, **39**, 354–364.

54 X. Liu, Z. Xu, A. Iqbal, M. Chen, N. Ali, C. Low, R. Qi, J. Zai and X. Qian, *Nano-Micro Lett.*, 2021, **13**, 54.

This journal is © The Royal Society of Chemistry 2025

Energy Environ. Sci., 2025, **18**, 7060–7070 | **7069**

55 Z. F. Sin, Q. Z. Yin, S. G. Zhou, H. Y. Chen, S. F. Wen, H. P. Yang, X. Y. Wu, J. H. Pan and Q. B. Zhang, *Adv. Energy Mater.*, 2025, 2500189.

56 Y. Yang, Z. Yang, Z. Li, J. Wang, X. He and H. Zhao, *Adv. Energy Mater.*, 2023, **13**, 2302068.

57 Z. Cao, X. Zheng, M. Zhou, T. Zhao, L. Lv, Y. Li, Z. Wang, W. Luo and H. Zheng, *ACS Energy Lett.*, 2022, **7** 3581–3592.

58 Y. Yu, C. Yang, Y. Jiang, Z. Shang, J. Zhu, J. Zhang and M. Jiang, *Adv. Energy Mater.*, 2024, **15**, 2403086.